

Controlling phonon lifetimes via sublattice disordering in AgBiSe₂

J. L. Niedziela ^{1,2,3,*} D. Bansal ² J. Ding,² T. Lanigan-Atkins,² C. Li,⁴ A. F. May ¹ H. Wang,¹ J. Y. Y. Lin ⁵
D. L. Abernathy ⁵ G. Ehlers,⁵ A. Huq,⁵ D. Parshall,⁶ J. W. Lynn ⁶ and O. Delaire ^{2,7,†}

¹Materials Science and Technology Division, Oak Ridge National Laboratory, Oak Ridge, Tennessee 37831, USA

²Department of Mechanical Engineering and Materials Science, Duke University, Durham, North Carolina 27708, USA

³Nuclear Nonproliferation Division, Oak Ridge National Laboratory, Oak Ridge, Tennessee 37831, USA

⁴Materials Science and Engineering, Department of Mechanical Engineering, University of California, Riverside, California 92521, USA

⁵Neutron Scattering Division, Oak Ridge National Laboratory, Oak Ridge, Tennessee 37831, USA

⁶NIST Center for Neutron Research, National Institute of Standards and Technology, Gaithersburg, Maryland 20899, USA

⁷Department of Physics and Department of Chemistry, Duke University, Durham, North Carolina 27708, USA



(Received 20 April 2020; accepted 4 August 2020; published 12 October 2020)

Understanding and controlling microscopic heat transfer mechanisms in solids is critical to material design in numerous technological applications. Yet, the current understanding of thermal transport in semiconductors and insulators is limited by the difficulty in directly measuring individual phonon lifetimes and mean free paths, and studying their dependence on the microscopic state of the material. Here we report our measurements of microscopic phonon scattering rates in AgBiSe₂, which exhibits a controllable, reversible change directly linked to microstructure evolution near a reversible structural phase transition, that directly impacts the thermal conductivity. We demonstrate a steplike doubling of phonon scattering rates resultant from the cation disordering at the structural transition. To rationalize the neutron scattering data, we leverage a stepwise approach to account for alterations to the thermal conductivity that are imparted by distinct scattering mechanisms. These results highlight the potential of tunable microstructures housed in a stable crystal matrix to provide a practical route to tailor phonon scattering to optimize thermal transport properties.

DOI: [10.1103/PhysRevMaterials.4.105402](https://doi.org/10.1103/PhysRevMaterials.4.105402)

I. INTRODUCTION

Gaining a microscopic understanding of heat transfer processes is critical for rationally designing materials in numerous technological applications, including thermoelectrics, thermal barrier coatings, semiconductors for microelectronics, and nuclear fuel. Thermoelectric materials enable direct conversion of thermal gradients into electrical energy, and they are sought in applications using natural or manmade heat sources [1–6]. Thermoelectric conversion efficiency is characterized by a figure of merit $zT = \alpha^2 \sigma T / \kappa_{\text{tot}}$, where α is the Seebeck coefficient, σ is the electrical conductivity, and κ_{tot} is the overall thermal conductivity of the material, itself the sum of lattice and electronic contributions, $\kappa_{\text{tot}} = \kappa_{\text{lat}} + \kappa_{\text{el}}$. This has prompted wide-ranging efforts to maximally suppress phonon propagation while preserving electronic mobility to maintain a high power factor $\alpha^2 \sigma$. Yet, while critical to benchmark phonon scattering theories, the experimental assessment of the lifetimes of individual phonon modes—in a momentum and energy resolved fashion—and their evolution as a function of temperature or sample conditions remains very challenging.

Semiconductors of the type ABX_2 (group I-V-VI₂) have previously been shown to exhibit an intrinsically low lattice

thermal conductivity, while achieving competitive power factors [7–9]. Examples include AgBiSe₂, NaSbSe₂, NaBiTe₂, NaSbTe₂, as well as AgSbTe₂, which has also successfully been alloyed with PbTe in the so-called LAST compound [10]. AgBiSe₂ is a promising thermoelectric material with zT approaching 1 near 800 K for n -type samples [11,12], and 1.5 at 750 K for nanostructured p -type samples [13], with a potential for room-temperature application [14]. The structure easily allows for doping and substitution, enabling tuning of transport properties [11–13,15,16].

The microscopic origin of the very low thermal conductivity in I-V-VI₂ semiconductors remains controversial. For example, Morelli *et al.* [8] argued that anharmonic phonon-phonon scattering was the dominant scattering mechanism in AgSbTe₂ and that the temperature-independent κ_{lat} would arise as a consequence of such a strong anharmonicity that the material was reaching the minimum possible thermal conductivity at all temperatures [8]. In contrast, neutron scattering investigations on AgSbTe₂ linked the observed T -independent phonon scattering rates to the emergence of a spontaneous nanostructure with short-range ordering on the cation sublattice [17–19], also observed by electron microscopy and scanning probe studies [20–23].

Although AgSbTe₂ exhibits cation short-range ordering on a pseudorocksalt lattice at all temperatures [17,18], AgBiSe₂ can be tuned with heat treatments to exhibit either disordered or long-range-ordered cations while preserving the crystallinity [15,24]. Thus, AgBiSe₂ provides a rare opportunity to directly investigate the role of cation disordering on

*niedzielajl@ornl.gov

†olivier.delaire@duke.edu

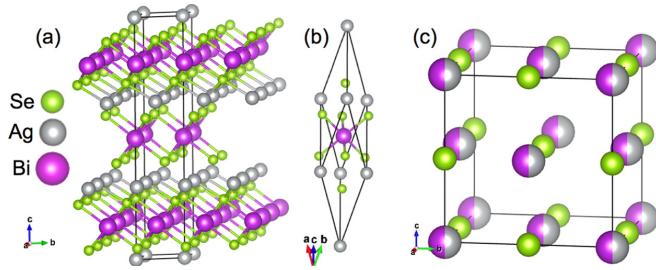


FIG. 1. Structure evolution of AgBiSe_2 . (a) Low-temperature ($T \leq 390$ K) α -phase. The Se layers alternate with layers of Bi and Ag. (b) Intermediate temperature ($393 \leq T \leq 560$ K) β -phase, which is a slightly distorted rhombohedral modification of the α -phase. (c) High-temperature rocksalt γ -phase, stable for $T \geq 560$ K, exhibiting a disordered distribution of Ag^+ and Bi^{3+} on the cation sublattice. The rocksalt cubic $\langle 111 \rangle$ directions yield the rhombohedral/hexagonal axes of β/α domains at low T .

the phonon scattering rates in a semiconductor by probing the dynamic behavior across the order-disorder transition. Here, we examine the phonon scattering mechanisms in AgBiSe_2 using neutron scattering, thermal diffusivity measurements, and first-principles calculations to understand the connection with the structural evolution. In particular, we performed inelastic neutron scattering (INS) measurements on large single crystals to extract quantitative information about the scattering rates, focusing on the transverse acoustic phonons that dominate the thermal conductivity.

AgBiSe_2 possesses three different crystalline phases depending on temperature [24,25], with distinct orderings of cations, as shown in Fig. 1. The high-symmetry rocksalt cubic γ -phase ($Fm\bar{3}m$, SG-225) is observed for $T \geq 560$ K [Fig. 1(c)], with Ag^+ and Bi^{3+} cations randomly distributed on a face-centered-cubic (fcc) sublattice and Se anions on their separate fcc sublattice. Between 393 and 560 K, the system adopts a rhombohedral β -phase ($R\bar{3}m$, SG-166), with segregation of the Ag and Bi ions into the $\langle 111 \rangle_{\text{cubic}}$ planes of the high-temperature γ -phase [Fig. 1(b)]. The low-temperature α -phase below 393 K, shown in Fig. 1(a), is hexagonal ($P\bar{3}m1$, SG-164), with Ag and Bi layers slightly displaced along the c -axis (along to $\langle 111 \rangle_{\text{cubic}}$) compared with the β -phase [25,26]. The fcc sublattice of Se from the rocksalt γ -phase is preserved through these phase transitions, but with slight distortions. Earlier transmission electron microscopy (TEM) work [24] showed that the microstructure of the room temperature and intermediate phases is comprised of twinned domains with different orientations of the rhombohedral/trigonal axis, corresponding to Ag/Bi layers orthogonal to different $\langle 111 \rangle_{\text{cubic}}$ directions. The twin domains in that study had a typical size of 50–100 nm, with a twinning microstructure expected to be dependent on thermal history.

The disordered rocksalt phase of AgBiSe_2 can be quenched after high-temperature annealing. This method was used for the TEM study in Ref. [24] and to compare the lattice thermal conductivity of the cubic and trigonal phases at cryogenic temperatures in polycrystalline material [9]. Lattice thermal conductivity measurements conducted this way are drastically different between trigonal AgBiSe_2 , which displays $\kappa_{\text{lat}} \sim$

T^{-1} characteristic of anharmonic scattering above a maximum at $T \sim 30$ K, and the quenched rocksalt AgBiSe_2 phase, which displays a glasslike, T -independent κ_{lat} between 10 and 300 K [9]. The thermal conductivity of quenched rocksalt AgBiSe_2 is similar to that of rocksalt AgSbTe_2 [9]. The annealed, long-range-ordered low-symmetry phase has larger thermal conductivity than the quenched phase at temperatures up to 300 K [9]. Thus, the degree of cation ordering is an effective way of controlling thermal conductivity in this system. While polycrystalline AgBiSe_2 can be quenched to retain the rocksalt disordered phase, single crystals shatter upon quenching, thus we studied cation disordering on heating across the ordered rhombohedral to disordered rocksalt transition instead.

INS is a powerful experimental probe of phonons in materials. While optical spectroscopies provide high-resolution phonon spectra, they are limited to modes at (or near) the Brillouin zone center and are limited by selection rules. In contrast, INS can access phonon modes across the entire Brillouin zone, with energy, momentum, and eigenvector polarization selectivity. By combining measurements of powder and single-crystal samples, we probed both the phonon density of states (DOS) as well as the temperature-dependent phonon dispersions and linewidths, and we correlated our results with the structural evolution obtained from neutron diffraction.

Linewidths derived from INS measurements provide critical information about phonon scattering processes. Nevertheless, few INS investigations of phonon linewidths in thermoelectrics have been reported to date [17,18,27,28] because of the technical challenges of obtaining large single crystals, and the expertise needed for accurate corrections of complex resolution effects. For AgBiSe_2 , the energy widths of the transverse acoustic phonons are sufficiently broad that we can quantitatively extract linewidths along extended portions of the dispersion. To this end, we performed Monte Carlo modeling of the instrument resolution function [29] to deconvolve it from the linewidth.

Further, we exploit first-principles calculations to rationalize the phonon scattering mechanisms. Phonon simulations were done on several structures to evaluate the effects of cation ordering on phonon dispersions and thermal conductivity and to aid the INS interpretation. To understand the effect of cation ordering on phonon dispersions and the dynamical structure factor, we considered two variants of alloy structures including cubic D_4 and trigonal $L1_1$ [30]. Additional simulations were performed for the disordered γ -phase using a virtual crystal approximation (VCA) based on the rocksalt PbSe structure but using the average mass of Ag and Bi on the cation site and including effects of point-defect scattering. Thus, we determine the relative influence of anharmonic processes, mass disorder, and short-range ordering on phonon scattering rates to account for the low thermal conductivity of AgBiSe_2 .

II. METHODS

A. Single-crystal inelastic neutron scattering

For neutron scattering by harmonic phonons, which have infinitely long lifetimes, the coherent cross-section for

one-phonon emission is given by [31]

$$\begin{aligned} \left(\frac{d^2\sigma}{d\Omega dE} \right)_{\text{coh}} &= \frac{k'}{k} \frac{(2\pi)^3}{2v_0} \Sigma_s \Sigma_\tau \frac{1}{E_s} \\ &\times \left| \Sigma_d \frac{\bar{b}_d}{\sqrt{M_d}} \exp(-W_d) \exp(i\mathbf{Q} \cdot \mathbf{d}) (\mathbf{Q} \cdot \mathbf{e}_{ds}) \right|^2 \\ &\times \langle n_s + 1 \rangle \delta(E - E_s) \delta(\mathbf{Q} - \mathbf{q} - \boldsymbol{\tau}) \\ &= \frac{\sigma_{\text{coh}} k'}{4\pi k} NS(\mathbf{Q}, E), \end{aligned} \quad (1)$$

where k' and k are the final and incident neutron wave vector, \mathbf{q} is the phonon wave vector, E_s is the eigenvalue of the phonon corresponding to the branch index s , \mathbf{e}_{ds} is the phonon eigenvector, $\boldsymbol{\tau}$ is the reciprocal-lattice vector, d is the atom index in the unit cell, \mathbf{d} is the atomic position in the unit cell, \bar{b}_d is the average scattering length for atom d , M is the atomic mass, W is the corresponding Debye-Waller factor, \mathbf{Q} is the wave-vector transfer, and $S(\mathbf{Q}, E)$ is the dynamical structure factor. Phonon scattering processes lead to finite lifetimes, $\tau_{\mathbf{q},j}$, and as a consequence the phonon spectral functions $A_{\mathbf{q},j}(E)$ are no longer δ functions, but they acquire a finite energy width (linewidth) [32–35]. In the weak scattering regime, the phonon spectral function can be described by a Lorentzian function, and the full width at half-maximum provides a measure of the mode-resolved scattering rate, $\tau_{\mathbf{q},j}^{-1}$ [33]. The dynamical susceptibility $\chi''(\mathbf{Q}, E)$ can be derived from $S(\mathbf{Q}, E)$ following

$$\chi''(\mathbf{Q}, E) = (1 - \exp\{-E/k_B T\}) S(\mathbf{Q}, E), \quad (2)$$

where E is the energy, k_B is the Boltzmann constant, and T is the temperature of the measurement.

We used high-quality single crystals (mass ~ 8 g), grown with a modified Bridgman method (details in the Supplemental Material [36]) and annealed *ex situ* in the α -phase for three weeks. All experiments were performed on this crystal using the thermal triple-axis spectrometer (TAX) BT-7 at the NIST Center for Neutron Scattering [37], the Wide Angular Range Chopper Spectrometer (ARCS) [38], and the Cold Neutron Chopper Spectrometer (CNCS) [39] time-of-flight (TOF) chopper spectrometers at the Spallation Neutron Source, in that order. While the cation transition is reversible, *in situ* heating cycles between the α - and γ -phases during multiple INS measurements could affect the sample microstructure, as it is not possible to anneal *in situ* as long as during sample preparation. For this reason, a second crystal, annealed *ex situ* in the α -phase, was measured (CNCS) for comparison with the first crystal having undergone several *in situ* temperature cycles (BT-7, ARCS, CNCS). Our measurements show that the phonon spectra were not substantially affected by *in situ* thermal cycling.

For all INS measurements, crystals were mounted in the (HLL) scattering plane (pseudocubic notation) to provide access to high-symmetry directions. Scans of phonons were conducted at temperatures ranging between 50 and 690 K on BT-7. For the ARCS and CNCS measurements, the sample was mounted in a closed-cycle displac and measured at 300 and 640 K. At ARCS, the selected incident energy of 25 meV provided an elastic line energy resolution of 1.6 meV

decreasing to 1.3 meV at 5 meV energy transfer [40], and a rotating collimator was used to reduce the scattering background [41,42]. For the CNCS measurements, an incident energy of 15 meV was used, which provides an estimated elastic line energy resolution of 0.7 and 0.4 meV at 5 meV energy transfer. For TOF INS measurements, the crystal was rotated through a large angular range in 1 degree steps, mapping the four-dimensional $S(\mathbf{Q}, E)$ for a large number of Brillouin zones. Data were reduced using MANTID algorithms [43], and analyzed using HORACE [44]. These single-crystal measurements enabled detailed investigation of both low-energy phonons and elastic scattering. Further details of INS experiments including temperature correction information are provided in the Supplemental Material [36].

B. Powder INS

For single-phonon scattering in a polyatomic material, the inelastic neutron scattering cross-section is proportional to the scattering function, which is closely related to the phonon DOS in the case of incoherent scattering:

$$S_{\text{inc}}(\mathbf{Q}, E) = \sum_i \sigma_i \frac{\hbar^2 Q^2}{2M_i} \exp(-2W_i) \frac{g_i(E)}{E} [n_T(E) + 1], \quad (3)$$

where \mathbf{Q} and E are the momentum and energy transfer to the sample; $Q = |\mathbf{Q}|$, σ_i , M_i , and $\exp(-2W_i)$ are the neutron scattering cross-section, mass, and Debye-Waller factor for atom i , respectively; and $n_T(E)$ is the Bose occupation factor [31].

The partial phonon DOS, g_i , is defined as

$$g_i(E) = \sum_{j,\mathbf{q}} |e_i(j, \mathbf{q})|^2 \delta[E - E(j, \mathbf{q})], \quad (4)$$

where $E(j, \mathbf{q})$ and $\mathbf{e}(j, \mathbf{q})$ are the phonon energies and eigenvectors [31,45]. As can be seen from Eq. (3), the measured INS signal (in the incoherent approximation) provides a neutron-weighted approximation to the DOS, with the spectral contributions from each species i corresponding to its partial phonon DOS g_i , weighted with $\exp(-2W_i)\sigma_i/2M_i$. The Debye-Waller factors for each species are close to unity, however the ratios of neutron cross-sections and masses differ substantially: 0.046 for Ag, 0.0438 for Bi, and 0.105 for Se, making contributions from Se motion dominant in the neutron-weighted DOS.

To determine the DOS, time-of-flight INS data were collected on an 8 g powder sample of AgBiSe₂ using ARCS [38,46]. The sample had been annealed for 72 h prior to the measurements, providing access to the long-range-ordered phase. Data were collected with incident neutron energies $E_i = 15$ and 40 meV. At $E_i = 40$ meV, the estimated energy resolution at the elastic line (zero-energy transfer) was 2.5 meV, which decreases to 0.7 meV at 18 meV. A background measurement from an empty Al can was measured in identical conditions. The data were reduced using MANTID algorithms [43] and analyzed in the incoherent approximation to obtain the phonon DOS, following a standard procedure [47]. Data are then corrected for neutron weighting effects, as described in the Supplemental Material Ref. [36].

C. Time-of-flight neutron powder diffraction

Time-of-flight neutron diffraction data were obtained using the POWGEN instrument [48] at the Spallation Neutron Source. The temperature evolution of the structure and the effect of disordering was studied from 100 to 600 K. Lattice parameters were extracted from LeBail and Rietveld refinements performed with GSAS [49]. Additional data and temperature correction information are discussed in the Supplemental Material.

D. First-principles simulations

Phonon simulations were performed on several structure variations of AgBiSe₂ to evaluate the effects of cation ordering on the phonon dispersions and thermal conductivity. First-principles simulations were performed in the framework of density functional theory (DFT) as implemented in the Vienna *abinitio* Simulation Package (VASP 5.3) [50–52]. We used a $6 \times 6 \times 6$ Monkhorst-Pack electronic k -point mesh with a plane-wave cutoff energy of 300 eV in all of our simulations. The convergence criterion for the electronic self-consistent loop was set to 10^{-8} eV. The projector-augmented-wave potentials explicitly included 11 valence electrons for Ag, five for Bi, and six for Se. We used both the local density approximation (LDA) [53] and the Perdew-Burke-Ernzerhof (PBE) functional [54] for the exchange correlation functional. During the relaxation of the structure, the lattice parameters and atomic positions were optimized until forces on all atoms were smaller than $1 \text{ meV } \text{\AA}^{-1}$. We considered two variants of alloy structures D_4 (also known as AF-IIb, space group no. 227) [30] and $L1_1$ (also known as AF-Ib, space group no. 166) to describe the Ag/Bi ordering as shown in Fig. 1 of the Supplemental Material Ref. [36]. Due to the difficulty in capturing the site-disordering of the Ag-Bi atoms induced by the phase transition, we use these two variants to assess changes in the phonon-dispersion relations induced by different local orderings of cations. Further simulations were performed on the VCA of the rocksalt phase.

For all phases, phonon dispersions were calculated in the harmonic approximation using the finite displacement approach as implemented in PHONOPY [55]. The atomic displacement amplitude was 0.01 \AA . Both LDA and PBE calculations resulted in stable phonons, albeit with slightly higher energies for modes calculated with LDA, which is consistent with the smaller lattice parameter obtained for the structure during relaxations when using the LDA functional.

E. Thermal transport characterization

Flash thermal diffusivity was used to characterize thermal conductivity above room temperature. The experimental thermal conductivity is calculated as $\kappa = \rho C_p D$, where ρ , C_p , and D are the density, heat capacity, and thermal diffusivity. Thermal diffusivity measurements were performed with a Netzsch LFA-457 laser flash apparatus from 300 to 700 K on an annealed slice cut from a polycrystalline ingot.

III. RESULTS

We start with a discussion of the phonon behaviors from the temperature-dependent INS measurements. An overview

of the dispersions determined with TOF-INS and DFT calculations convoluted with the experimental energy resolution and neutron weighting [56] is provided in Fig. 2, experimental results from TAX-INS are given in Fig. 3, and the phonon DOS from experiment and calculation is shown in Fig. 4.

The acoustic branches of AgBiSe₂ are similar in energy and shape to those measured in AgSbTe₂ [17,18], with the [1,1,0]-polarized TA branch propagating along [0,0,1] reaching up to $\sim 4.7 \text{ meV}$ at the zone boundary at 300 K [Fig. 2(a)], and the [0,0,1]-polarized TA branch along [1,1,0] reaching around 6 meV at the top at 300 K [Figs. 3(d) and 2(b)]. The top of the longitudinal acoustic (LA) modes is difficult to discern due to their broadening and merging with optical modes.

The optical modes in AgBiSe₂ extend up to $\sim 22 \text{ meV}$ at 300 K, as seen in the phonon DOS [Fig. 4(e)], while the DOS only reaches about 20 meV in AgSbTe₂ at the same temperature. This can be explained by the lighter mass of Se compared with Te. In addition, in AgBiSe₂ the acoustic modes, below 12 meV , are better separated from the optic modes (spectral peak at $15 < E < 22 \text{ meV}$ in the DOS) than in AgSbTe₂, which exhibits a large peak of mixed nature in the DOS at $\sim 13 \text{ meV}$. This arises from the larger mass ratio between cations and anions in AgBiSe₂. Well-defined phonon peaks are seen at 7, 10, 17, and 20 meV in the measurement at 50 K. With increasing temperature, all the features in the DOS tend to broaden, and a distinct shift to lower energy (“softening”) can be observed for higher-energy peaks.

We now discuss the temperature dependence of the thermal diffusivity and INS measurements. Diffusivity results shown in Fig. 5 reflect a gradual decrease on heating from 300 to 500 K, consistent with increased anharmonic phonon scattering, with little change across the α - β transition, as expected considering the limited structural change between these two phases, and their compatible domain structures [24]. On the other hand, a strong suppression of the diffusivity is observed from the β - to the γ -phase across T_{od} . While the origin of the spike at 525 K is not obvious, a clear steplike drop is observed across the disordering process at $\sim 550 \text{ K}$, qualitatively consistent with reports on annealed samples [9]. The diffusivity at room temperature at the end of the cooling cycle is 15% lower than the original starting value, reflecting strong thermal hysteresis, likely resulting from partial quenching of the disordered γ -phase.

The rhombohedral transition appears to depress the number of phonon modes near 10 meV reflected by the decreasing DOS weight near 10 meV , while the transition to the γ -phase results in the broadening of the high-energy modes involving Se, merging the peaks at 17 and 20 meV . Nevertheless, the mean energy of the DOS remains approximately constant. The average phonon energy $\langle E \rangle$ is obtained from the neutron-deweighted DOS (Fig. 4), and at 50 and 640 K we find $\langle E \rangle = 13.6$ and 12.8 meV , respectively, corresponding to Debye temperatures of 210 ± 2 and $198 \pm 2 \text{ K}$. This relatively small change indicates little change in the overall bonding strength and resulting force constants across this temperature range.

We note that the $\beta \rightarrow \gamma$ phase transition is reflected quite strongly in the momentum-resolved phonon measurements. Both the TA and LA phonons in AgBiSe₂ experience substantial softening and linewidth broadening with increasing

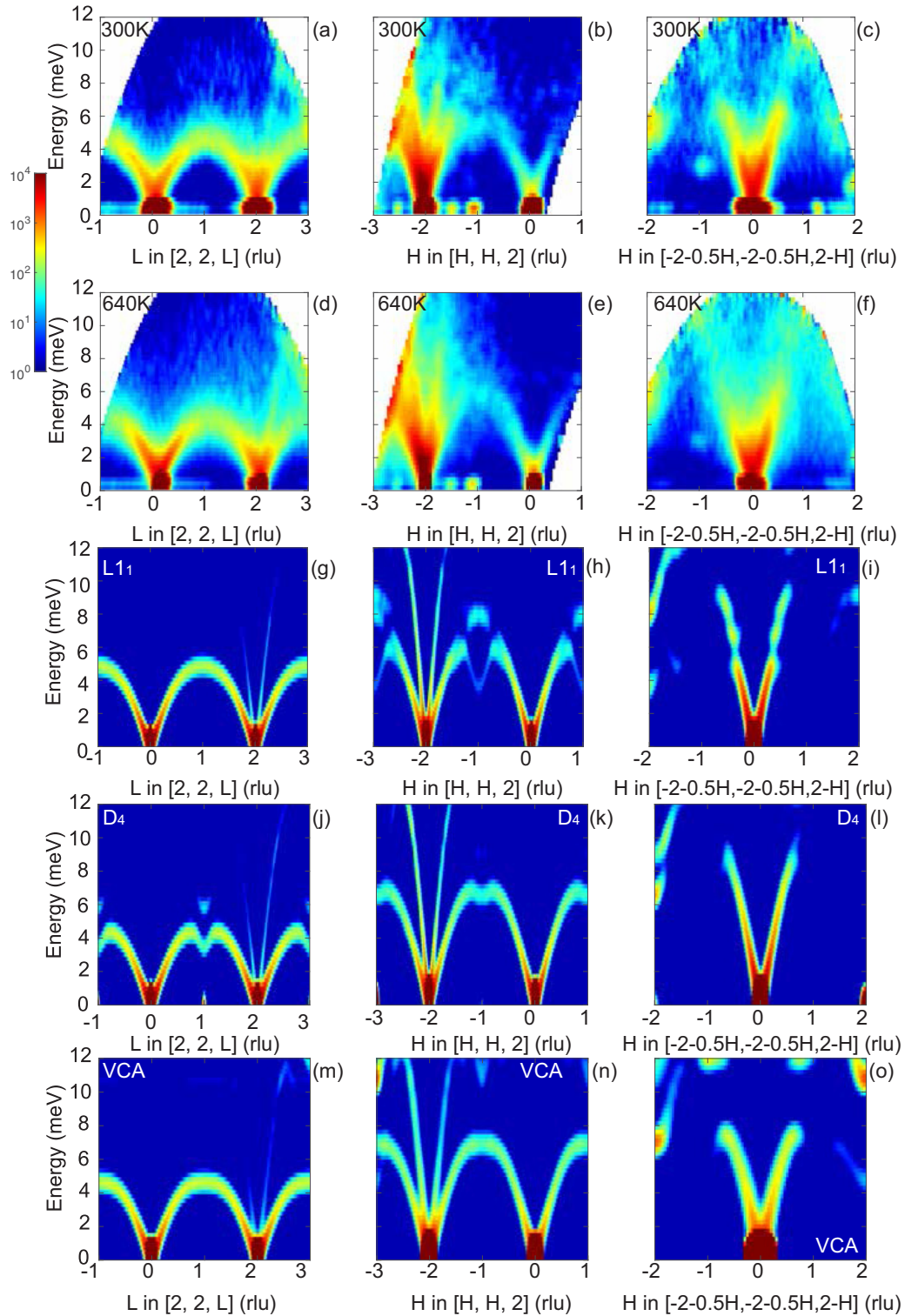


FIG. 2. Dynamic susceptibility $\chi''(\mathbf{Q}, E)$ of AgBiSe_2 measured at 300 K (a)–(c) and 640 K (d)–(f) with CNCS, along reciprocal space directions: (a,d) $(2, 2, 0) + (0, 0, \xi)$, (b,e) $(0, 0, 2) + (\xi, \xi, 0)$, and (c,f) $(-2, -2, 2) + (-0.5\xi, -0.5\xi, -\xi)$. Scattering intensity maps are obtained by integrating in ± 0.1 r.l.u. in orthogonal directions. (g)–(o) Simulated $\chi''(\mathbf{Q}, E)$ along corresponding directions, for the $L1_1$ (g,h,i), D_4 (j,k,l) ordered structures, and a VCA structure (m,n,o). The VCA model is based on rocksalt PbSe , replacing the mass of Pb with the average mass of Ag and Bi . In all panels, the logarithmic intensity scale spans four orders of magnitude.

temperature prior to the transition, with a sharp increase in the phonon linewidths at the structural transition. Representative constant- Q scans from INS are shown in Fig. 3. Figures 3(a) and 3(b) show the behavior of the transverse acoustic mode at

(a) the Brillouin zone boundary along the Γ - X direction, and (b) the temperature evolution at the midpoint in that direction. A drastic broadening of optical modes on heating from the $\alpha \rightarrow \beta$ and $\beta \rightarrow \gamma$ phases is particularly notable. Figures 3(c)

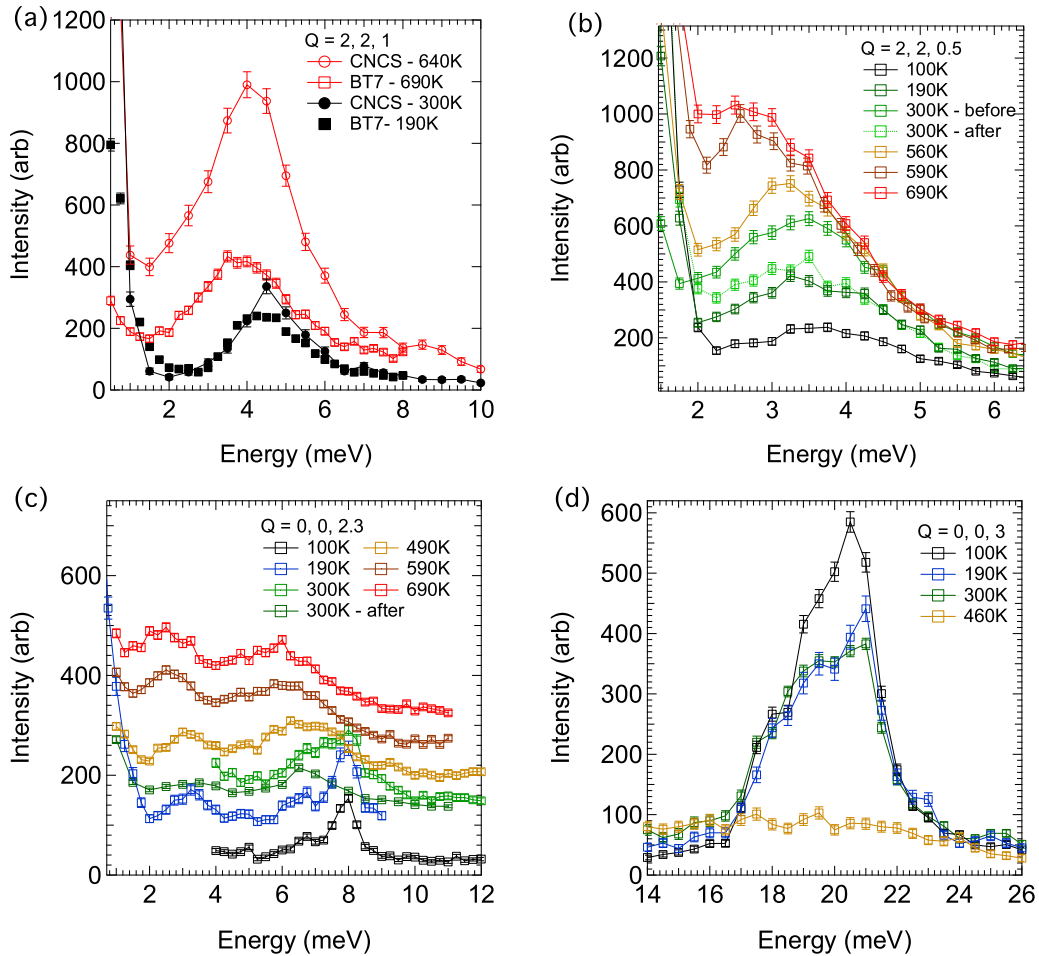


FIG. 3. Representative constant- Q data for AgBiSe_2 . (a) $S(E)$ for scans at $\mathbf{Q} = (2, 2, 1)$ showing the softening and broadening on warming of the transverse acoustic mode at the Brillouin zone boundary. (b) $S(E)$ for scans at $\mathbf{Q} = (2, 2, 0.5)$ showing the softening of the transverse acoustic mode near the Brillouin zone midpoint. (c) Temperature evolution for $\mathbf{Q} = (0, 0, 2.3)$ showing a longitudinal optic mode and parasitic transverse mode, which both show broadening on warming. (d) Longitudinal acoustic mode at $\mathbf{Q} = (0, 0, 3)$ showing the complete damping of high-energy optical modes in the β -phase.

and 3(d) show longitudinal scans at $\mathbf{Q} = (0, 0, 2.3)$, an intermediate location along the Γ - X direction, and $\mathbf{Q} = (0, 0, 3)$, corresponding to the Brillouin zone boundary along Γ - X . Figure 3(d) shows a well-defined LO mode at ~ 20 meV for $T < 300$ K, an energy in good agreement with our LDA simulations and the top of the measured phonon DOS. Strikingly, this mode essentially disappears at $T = 460$ K (β -phase). Similarly, the LA mode at $\mathbf{Q} = (0, 0, 2.3)$ shows a well-defined peak at 8 meV in scans at $T = 100, 190, 300$ K in the annealed α -phase, but it becomes drastically broader on heating into the β - and γ -phases. Its energy also drops considerably, from 8 to 7 meV across the $\alpha \rightarrow \beta$ transition, and further from 7 to 6 meV across $\beta \rightarrow \gamma$ ($T \geq 560$ K). The TA mode at about 3 meV is parasitically seen in this longitudinal scan, and its energy is seen to decrease with increasing T as well, but this scattering condition cannot resolve the TA linewidth appropriately. We note that upon cooling back to room temperature *in situ*, the LA mode remains broad, and centered at ~ 6.5 meV, which indicates that the cation disorder is likely partly quenched and corroborates strong thermal hysteresis observed in diffusivity measurements (Fig. 5).

Maps of $S(\mathbf{Q}, E)$ obtained from CNCS on the crystal previously measured with BT-7 are shown in Figs. 2(a)–2(f) for the reciprocal space directions (22ξ) , $(\xi\xi 2)$, and $(1, 1, -1) + (\xi\xi\xi)$ at 300 and 640 K. A softening of the phonon dispersions is readily visible in Fig. 2, and the broadening of the phonon peaks is most apparent along the $[2, 2, L]$ direction. Further $S(\mathbf{Q}, E)$ maps obtained from measurements with ARCS, covering a wider range of phonon energies, are shown in Fig. 5 of the Supplemental Material Ref. [36], showing substantially reduced intensity in the optical modes. Figure 2 also shows comparisons between the INS data and the $S(\mathbf{Q}, E)$ calculated from our DFT simulations of phonons for different ordered structures ($L1_1, D_4$), as well as the VCA based on the rocksalt model of the disordered γ -phase. Agreement between the experimental data and simulations is reasonable (Fig. 2), with simulations slightly underestimating the TA phonon frequencies, as is evident in the comparison of the calculated phonon DOS to the experimentally derived values shown in Fig. 4.

The acoustic branch intensities and energies along the three directions shown in Fig. 2 are faithfully reproduced overall. Changes in the TA dispersion along $[H, H, 2]$ are seen between 300 and 640 K. Two modes are seen near $H = -1$

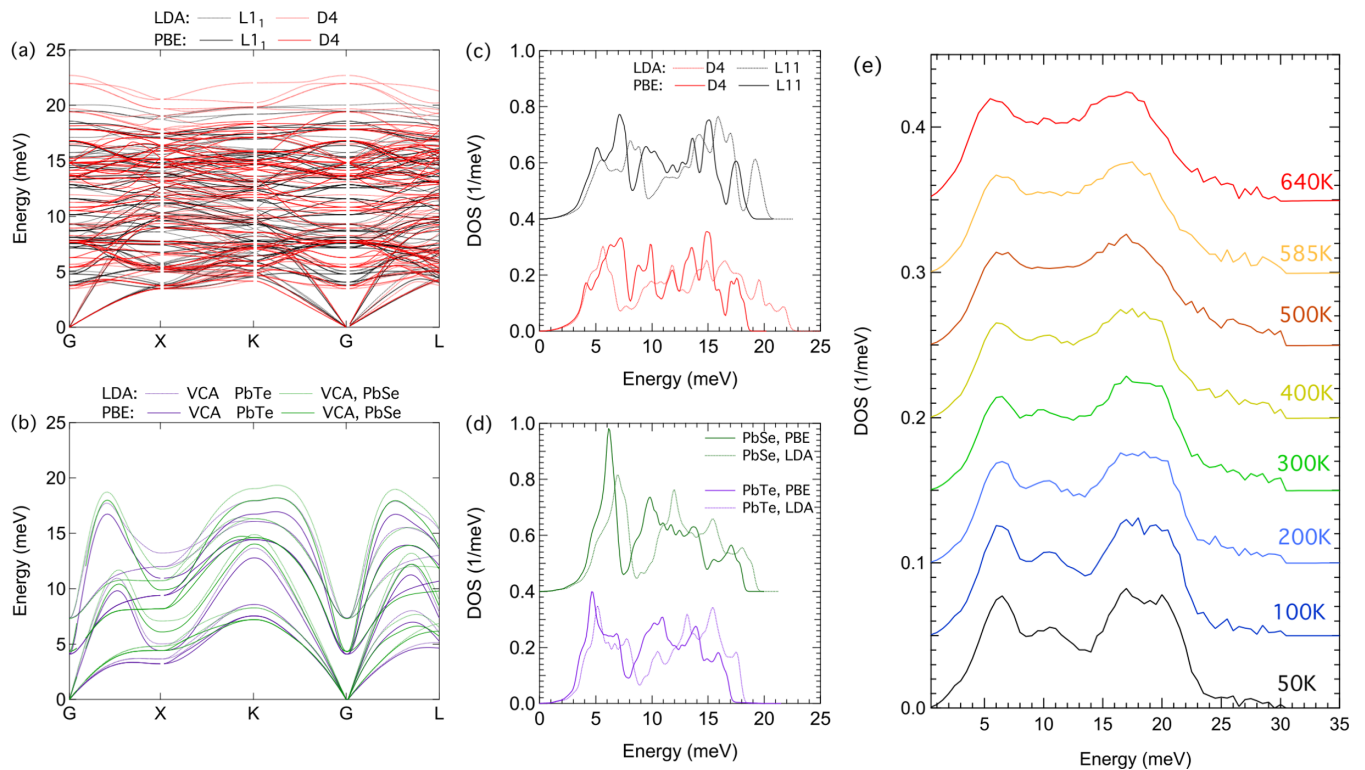


FIG. 4. (a) Phonon dispersions calculated from alloy variant structures. (b) Phonon dispersions of PbSe and PbTe. (c) DOS calculated for alloy variants. (d) DOS calculated for PbSe and PbTe. (e) Neutron deweighted phonon DOS on heating from 10 to 640 K. In (a)–(d) solid lines correspond to values determined using PBE, while dotted lines correspond to values determined using LDA.

at 5.5 and 8 meV at 300 K, due to a low-energy transverse optic branch. The intensity pattern is better reproduced by the $L1_1$ simulation, which features alternate layers of Ag and Bi cations, than by the cubic D4 structure. This feature is clearly associated with cation ordering, as it disappears in the INS data for the γ -phase at 640 K, in good agreement with the rocksalt VCA simulation. This confirms the observation in BT-7 data of the disappearance in the γ -phase of some optic modes associated with the cation ordering [Fig. 3(a)]. The

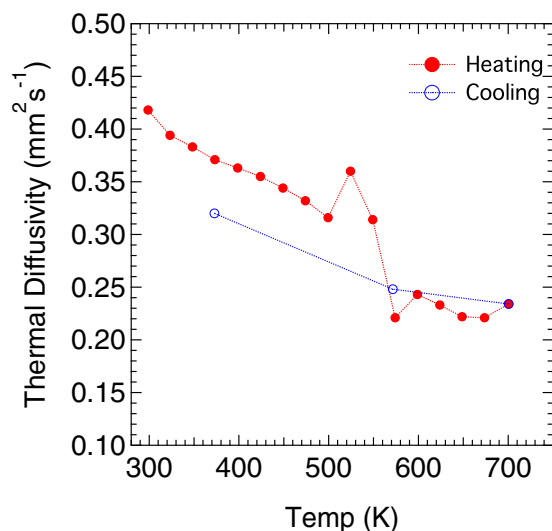


FIG. 5. Thermal diffusivity obtained on heating (red) and cooling (blue).

300 K INS data along $[2, 2, L]$ also agree better with the $L1_1$ model than the D4 simulation (no dip in the TA mode near $L = 1$).

From single-crystal INS data, we extracted the phonon linewidths after corrections for instrument resolution effects. The results for the intrinsic energy and \mathbf{Q} resolution for the CNCS spectrometer along high-symmetry paths for the transverse acoustic modes in AgBiSe_2 propagating along $\Gamma \rightarrow X$ and $\Gamma \rightarrow K$ were calculated using the Monte Carlo (MC) simulation and instrumental settings. BT-7 resolution was modeled using the Popovici method [57] using RESLIB as implemented in RESLIBCAL [58] with the appropriate instrument configuration. Additional details on the resolution modeling are given in the Supplemental Material Ref. [36].

We now present the temperature dependence of the phonon energy and linewidth of the TA mode at $\mathbf{Q} = (2, 2, 1)$. In the cubic description, this wave vector corresponds to the zone boundary at the X point (reduced phonon wave vector $\mathbf{q} = [0, 0, 1]$), and the intensity is from the TA mode polarized along $[1, 1, 0]$. This point provided the most accurate determination of the phonon energy and linewidth, as it corresponds to the relatively flat portion of the TA branch with low group velocity, and is less sensitive to the sample mosaic. Results are shown in Fig. 6(a) comparing BT-7 (black markers) and CNCS measurements (red markers) on heating. The linewidths extracted from INS data are in excellent agreement between the two instruments. Both the energy and linewidth of the TA phonon mode exhibit a dramatic change across the order-disorder phase transition at 560 K. The mode energy is relatively constant at $T \leq 300$ K, but it exhibits a

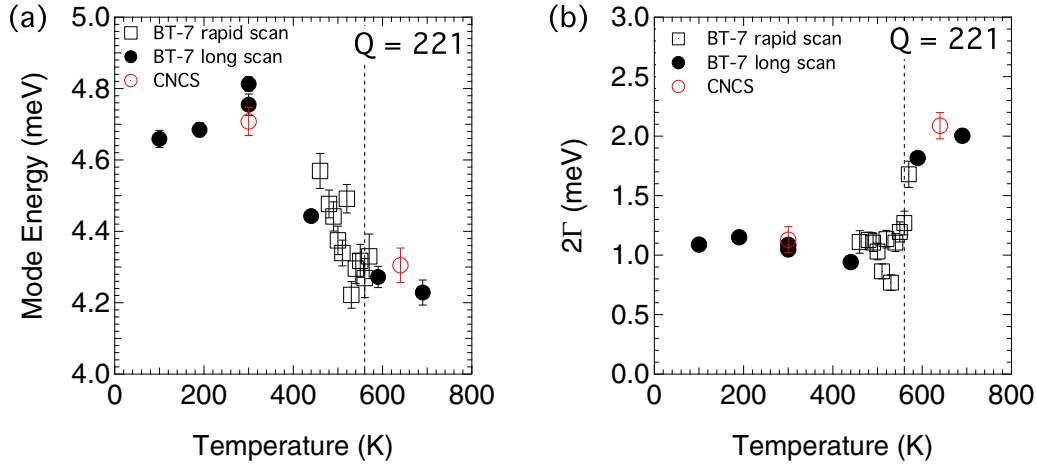


FIG. 6. TA mode energy (a) and phonon scattering rate (b) as a function of temperature on heating derived from constant Q scans at $Q = (2, 2, 1)$ for BT-7 (black markers) and CNCS (red markers). The measurement point corresponds to the Brillouin zone boundary at the X point in the (00ξ) direction. Fits for BT-7 data are performed in the single-mode analysis regime in convolution with the experimental resolution function. Error bars are one standard deviation of the fitting parameter. Vertical dotted line indicates the reported $\beta \rightarrow \gamma$ phase-transition temperature of 560 K.

clear softening of about 10% on warming into the disordered γ -phase. The behavior of the phonon linewidth is most striking, with a large steplike increase from ~ 1 meV in the α - and β -phases to ~ 2 meV upon warming into the γ -phase. This represents a doubling of the phonon-scattering rate in the cation-disordered γ -phase, compared with the long-range-ordered β - and α -phases. We have previously shown in the related AgSbTe_2 compound that TA modes dominate thermal transport. This strong increase in phonon scattering rates at the order-disorder transition is thus consistent with the large suppression in thermal conductivity at about 550 K reported in Refs. [11,12], and is consistent with our thermal diffusivity results shown in Fig. 5.

We now discuss the temperature-dependent atomic structure of AgBiSe_2 , probed with both powder neutron diffraction and energy-resolved TOF measurements on single crystals. Powder diffraction data allow us to track the average crystal structure (see the Supplemental Material Ref. [36]). The single-crystal data further reveal weaker diffuse scattering between the Bragg peaks from short-range correlations in the high-temperature phase, in addition to long-range ordering observed in the low-temperature phase. Figure 7 shows the elastic diffuse scattering obtained by energy filtering the INS data ($-1 < E < 1$ meV), revealing diffuse scattering from time-averaged spatial correlations. The energy filtering allows us to remove the thermal diffuse scattering from phonons, which is an otherwise prominent source of diffuse scattering in this system, similar to the case of AgSbTe_2 [18].

Figures 7(a) and 7(c) reveal the development of a superstructure due to the ordering of Ag and Bi cations in the low- T rhombohedral structure (rows of weak reflections along $\langle 111 \rangle_{\text{cubic}}$), in agreement with results from TEM [24], and also observed in our powder neutron diffraction data (see the Supplemental Material Ref. [36]). We also observe a longitudinal peak splitting of (222) Bragg peaks due to the symmetry lowering in the low-temperature phase, also in agreement with the powder measurements (see the Supplemental Material Ref. [36]). In addition, we note that

the multiple possible rhombohedral twin domains appear with equal likelihood, resulting in similar intensities for superstructure peaks along different $\langle 111 \rangle_{\text{cubic}}$ directions. The superstructure Bragg peaks disappear upon heating into the disordered rocksalt phase, as demonstrated in Figs. 7(b) and 7(d). We note that the order-disorder transition was reversible and reproducible through multiple temperature cycles in the experiments performed on both powders and single crystals.

Noticeably, diffuse scattering intensity [Figs. 7(b) and 7(d)] remains (along $\langle 111 \rangle_c$) even above T_{od} , revealing retained short-range order. Importantly, the long-range ordering of cations into rhombohedral domains below T_{od} occurred on a relatively fast time scale (within minutes) in our centimeter-size AgBiSe_2 sample. This behavior is quite different from our observations in AgSbTe_2 , which did not become long-range-ordered even upon annealing, although the short-range ordering in AgSbTe_2 was pronounced and obvious in neutron, x-ray, and electron diffraction [17,18,20]. The correlation length for cation short-range order in nominally rocksalt AgSbTe_2 was estimated to be a few nanometers [17,18]. To characterize the correlation length in the high-temperature rocksalt γ -phase of AgBiSe_2 , we considered linear cuts of the data along the L direction by integrating the $[HH0]$ axis and fit the resulting broad peaks to Gaussians. The full widths at half-maximum of the diffuse scattering peaks are 0.43(5) and 0.69(5) reciprocal-lattice units (r.l.u.), thus making them comparable in size to nanoscale correlations observed in AgSbTe_2 [18]. At temperatures much higher than T_{od} , we expect weakening cation short-range order. We can thus further corroborate our suggestion that the strong increase in phonon scattering at 550 K in Fig. 6(b) arises from the disordering of Ag/Bi cations on their sublattice, which retains some degree of nanoscale short-range correlations of cations.

The study of thermal conductivity in AgSbTe_2 by Morelli *et al.* pointed to anharmonic scattering suppressing κ_{lat} to the minimum bound theorized by Slack and Cahill [8]. However, sound velocities used in that study were overestimated by

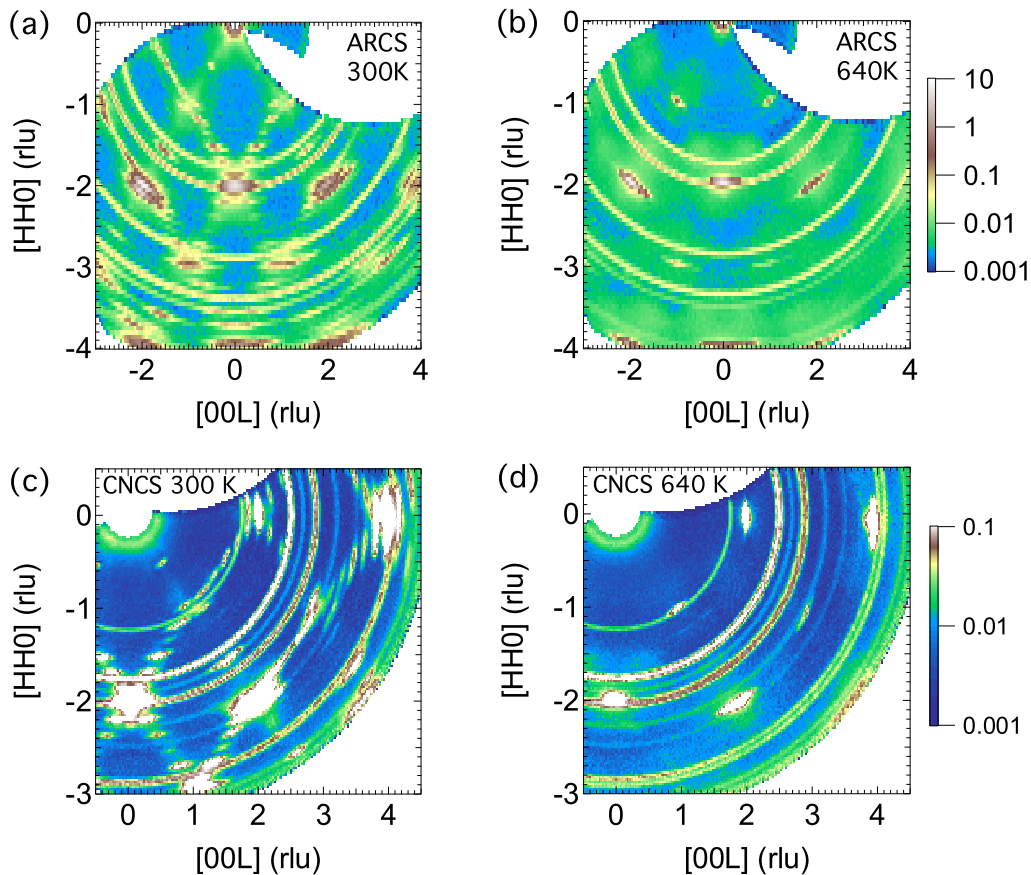


FIG. 7. Elastic intensity measured on AgBiSe_2 at (a) 300 K and (b) 640 K in the HHL plane with ARCS ($-2 < E < 2$ meV), and CNCS at (c) 300 K and (d) 640 K ($-1 < E < 1$ meV). In all cases, the intensity is integrated over $-0.1 \leq K \leq 0.1$ in the out-of-plane $[K, -K, 0]$ direction. The superstructure from long-ranged cation ordering appears as rows of reflections along $\langle 111 \rangle_{\text{cubic}}$ in the trigonal phase at 300 K (a,c), but is absent at 640 K (b,d). At 640 K, patches of diffuse scattering remain, indicative of cation short-ranged order. Diffraction rings are from the polycrystalline Al sample holder, with some sample contributions. Colors are shown on a log scale, and the color bars from panels (b) and (d) refer to ARCS and CNCS data, respectively.

a factor of almost 3, compared with recent neutron scattering measurements of acoustic phonon dispersions and resonant-ultrasound measurements [17], leading to a significant overestimation of the minimum κ_{lat} .

From neutron scattering, x-ray scattering, electron microscopy, and scanning probe microscopy, a short-range ordering of Ag^+ and Sb^{3+} on the cation sublattice was identified in AgSbTe_2 [17,18,20–23], and this nanometer-scale inhomogeneity was shown to strongly scatter the phonons in a temperature-independent fashion. The short-ranged order and additional point defects in AgSbTe_2 may be the result of structural frustration due to an inherent nonstoichiometry (composition close to $\text{Ag}_{22.2}\text{Sb}_{26.8}\text{Te}_{51}$). On the other hand, AgBiSe_2 forms more readily at the stoichiometric composition [16,59].

The κ we measured in AgBiSe_2 is very low (Fig. 8), about $0.68 \text{ W m}^{-1} \text{ K}^{-1}$ at 300 K decreasing slowly to $0.46 \text{ W m}^{-1} \text{ K}^{-1}$ at 700 K. Our κ measurements are in good agreement with previous reports obtained on a quenched pseudorocksalt sample in the temperature region over which they overlap (300–400 K) [8,9]. The large change in phonon linewidth on warming across the order-disorder transition observed in our INS measurements of AgBiSe_2 is expected to

directly correlate with a suppression of κ_{lat} . Indeed, our thermal diffusivity measurements show a pronounced suppression in the disordered phase above approximately 550 K (Fig. 5).

To evaluate the importance of different phonon scattering mechanisms in AgBiSe_2 , we modeled κ_{lat} by incorporating results from our phonon measurements as well as our first-principles simulations. While the total thermal conductivity (κ) is the sum of lattice (κ_{lat}) and electronic (κ_{el}) components, the κ_{el} in AgBiSe_2 with rocksalt structure is several orders of magnitude smaller than κ_{lat} due to its very low σ [9], and it can be neglected. Consequently, we can compare the simulated κ_{lat} directly with our experimental values (for total κ) in Fig. 8. We consider the impact on κ_{lat} from several phonon scattering processes, in particular anharmonicity and scattering by disorder on the cation sublattice [60].

The κ_{lat} is calculated using a standard phenomenological model [60]:

$$\kappa_{\text{lat}} = \frac{1}{3} \sum_{\mathbf{q}, j} C_{v_{\mathbf{q}, j}} v_{\mathbf{q}, j}^2 \tau_{\text{total}, \mathbf{q}, j}, \quad (5)$$

where $C_{v_{\mathbf{q}, j}}$, $v_{\mathbf{q}, j}$, and $\tau_{\text{total}, \mathbf{q}, j}$ are the mode heat capacity, mode group velocity, and mode total scattering rate, respectively,

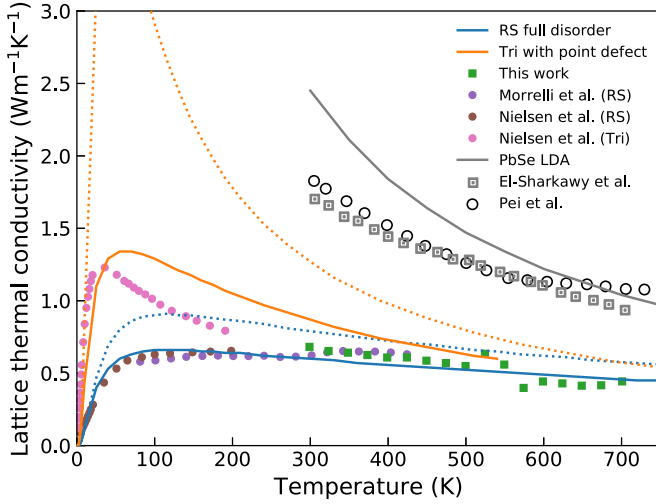


FIG. 8. Comparison of thermal conductivity models and experimental values. Markers represent our κ measurements (green squares), and reported κ for quenched sample with pseudorocksalt structure from Morrelli *et al.* (purple circles) [8] and Nielsen *et al.* [9], as well as the low-temperature ordered trigonal phase (pink circles) [9]. The κ_L obtained from our phenomenological model for the pseudorocksalt structure (see text) is shown as a blue line. The orange line shows κ_L for our model of the ordered $L1_1$ structure (see the text). Dotted lines represent a modified point-defect scattering model based on the expressions derived by Maris to take into account the shape of the DOS. The black circles and gray dotted squares show the measured values for PbSe [65,66], while the gray line represents our PbSe model.

and indices \mathbf{q} and j denote the phonon wave vector and branch number. Both $C_{v_{\mathbf{q},j}}$ and $v_{\mathbf{q},j}$ were determined by our DFT calculations of phonons based on the harmonic approximation [55].

Our analysis considers four distinct scattering processes: umklapp scattering (U), boundary scattering (B), as well as the effect of the random distribution of Ag and Bi on the cation sublattice (for the disordered rocksalt phase only), adding mass (M) and force-constant (FC) disorder:

$$\tau_{\text{total},\mathbf{q},j}^{-1} = \tau_{U,\mathbf{q},j}^{-1} + \tau_{B,\mathbf{q},j}^{-1} + \tau_{M,\mathbf{q},j}^{-1} + \tau_{FC,\mathbf{q},j}^{-1}. \quad (6)$$

The scattering rates are parametrized as follows (mode indices \mathbf{q} , j are left implicit):

$$\tau_U^{-1} = \frac{\hbar\gamma^2}{Mv^2\theta_D} \omega^2 T^n \exp(-\theta_D/bT), \quad (7)$$

$$\tau_B^{-1} = v/d, \quad (8)$$

$$\tau_M^{-1} = \frac{V}{4\pi v^3} \omega^4 \sum_i f_i \left(\frac{\bar{m} - m_i}{\bar{m}} \right)^2, \quad (9)$$

$$\tau_{FC}^{-1} = \frac{V}{2\pi v^3} \omega^4 \sum_i f_i \left(\frac{\bar{F} - F_i}{\bar{F}} \right)^2, \quad (10)$$

where \hbar is the reduced Planck constant, γ is the Grüneisen parameter, v is the group velocity, θ_D is the Debye temperature, ω ($E = \hbar\omega$) is the phonon frequency, d is the grain size, and V is the volume per atom. Here, M is the average atom mass, \bar{m} is the average mass of the disordered atoms, and \bar{F}

is the average self-force constant. Individual atoms of type i , with fraction f_i , have masses m_i and self-force constants F_i . We also evaluated the disorder scattering with the expressions derived by Maris [61]:

$$\tau_M^{-1} = \frac{\pi V \omega^2 D(\omega)}{6} \sum_i f_i \left(\frac{\bar{m} - m_i}{\bar{m}} \right)^2, \quad (11)$$

$$\tau_{FC}^{-1} = \frac{\pi V \omega^2 D(\omega)}{3} \sum_i f_i \left(\frac{\bar{F} - F_i}{\bar{F}} \right)^2, \quad (12)$$

where $D(\omega)$ is the phonon density of states per unit volume.

We start by modeling κ_{lat} for the ideal rocksalt system PbSe, which exhibits similar bonding characteristics to AgBiSe₂. This was motivated by our previous studies on phonons and thermal transport in AgSbTe₂ and PbTe [17,18,27], which showed that the ideal rocksalt system PbTe can be considered a virtual crystal approximant of the more complex AgSbTe₂ system (isostructural with AgBiSe₂), once the phonon frequencies are normalized for the mass effect. We performed harmonic DFT simulations of the PbSe phonon dispersions, and subsequently introduced umklapp and boundary scattering with the expressions given above. Using quasiharmonic phonon calculations for PbSe, we obtained an average $\gamma = 2.0$, in agreement with previous estimations of 1.65 and 2.23 [62,63]. The Debye temperature $\theta_D = 170$ K was estimated by $\frac{4\langle E \rangle}{3k_B}$ using the LDA phonon spectrum. We set the constant b as $2N^{1/3} = 4$, where N is the atom number in the conventional unit cell [64]. The constant n was set to 1.2. The value larger than 1 (pure umklapp processes) can be seen as representing the effect of phonon group velocity renormalization with temperature. As can be seen in Fig. 8, our model for κ_{lat} in PbSe matches the reported experimental values well at high temperature [65,66]. The larger discrepancy at low temperatures could result from underestimating anharmonicity or defects (or dopants), as κ_{lat} in PbSe is highly dependent on carrier concentration [67].

Next, to describe the disordered rocksalt phase of AgBiSe₂, we include the scattering rates τ_M^{-1} and τ_{FC}^{-1} associated with disorder on the cation sublattice. We introduce this disordered distribution of Ag⁺ and Bi³⁺ as a deviation from the VCA model based on PbSe, corrected for average cation mass $[(m_{\text{Ag}} + m_{\text{Bi}})/2]$. For AgBiSe₂, the reported γ varies from 1.6 [15] to 2.9 [9], which could originate from the error bars in experiments. To avoid introducing extra uncertainty, we kept the same $\gamma = 2$ and $n = 1.2$ as for PbSe. We set $\theta_D = 311$ K based on the mean phonon energy extracted from our AgBiSe₂ phonon DOS measurement. The mass of Pb²⁺ is heavier than the average mass of Ag⁺ and Bi³⁺, thus if we simply replace the Pb²⁺ in the VCA with the average mass of Ag⁺ and Bi³⁺, the resulting κ_{lat} is higher than PbSe (see the Supplemental Material Ref. [36]). Thus, disorder-induced scattering is quite significant to account for the κ_{lat} suppression in AgBiSe₂ compared to PbSe (see Fig. 8). This cation disorder in the high-temperature rocksalt phase is modeled with a 50% occupational disorder of Ag and Bi cations, namely $f_i = 0.5$ for both Ag and Bi. The atomic masses of Ag and Bi are 107.87 and 208.98 amu, respectively, leading to $\sum_i f_i \left(\frac{\bar{m} - m_i}{\bar{m}} \right)^2 = 0.102$. For τ_{FC}^{-1} , the self-force constants of Ag and Bi are 2.79 and 5.25 eV/Å²,

respectively (from D_4 LDA harmonic approximation), and $\sum_i f_i (\frac{\tilde{E}-E_i}{\tilde{E}})^2 = 0.094$. In addition, INS data revealed patches of diffuse scattering above T_{od} , indicating a residual cation short-range ordering over nanometers, providing a source of boundary scattering. Since the boundary scattering rate is directly proportional to the scattering length scale, by assuming 25% scattering chance by the 5 nm short-range ordering, an effective boundary scattering length of 20 nm was used. The combined effects of τ_M^{-1} , τ_{FC}^{-1} , and τ_B^{-1} significantly suppress κ_{lat} in disordered AgBiSe₂ (Fig. 8, blue line), yielding a result that matches our measurements at high T (green squares) as well as prior reports on quenched samples of the disordered rocksalt phase (purple and brown dots) [8,9].

We similarly estimated κ_{lat} for the ordered $L1_1$ structure, using the phonon dispersions from our quasiharmonic DFT simulations of the $L1_1$ phase. The boundary scattering length was set to be 100 nm as observed by TEM [24], and we applied a small fraction of point-defect scattering [$\sum_i f_i (\frac{\tilde{m}-m_i}{\tilde{m}})^2 = 0.02$]. The calculated κ_{lat} for this long-range-ordered phase (featuring little cation disorder) roughly follows a $1/T$ behavior for $T > 30$ K, indicating that the dominant scattering process is anharmonic umklapp scattering, as expected. The result is shown in Fig. 8 (orange line) and qualitatively reproduces the trend reported by Nielsen *et al.* for the annealed AgBiSe₂ samples in the trigonal structure (pink dots). While the agreement for the $L1_1$ ordered phase is only qualitative, our analysis does capture the strong κ_{lat} suppression in the quenched disordered rocksalt phase, especially below 300 K (blue versus orange lines) and the weak temperature dependence in that phase. While the second model of disorder scattering (Maris) gives a slightly larger κ_{lat} , the agreement with experiments remains fair, and the strong suppression upon cation disordering is preserved. Our thermal conductivity analysis thus supports our observations from INS measurements that phonons are strongly scattered by the disordering of Ag⁺ and Bi³⁺ on the cation sublattice.

IV. CONCLUSIONS

In summary, neutron scattering measurements have been carried out to assess the structure and dynamics of AgBiSe₂ across the cation order-disorder transition at $T_{od} \approx 550$ K. Substantial changes in phonon scattering rates are observed at the transition, with the extracted TA linewidths doubling upon heating into the high-temperature disordered γ -phase, consistent with an observed drop in the measured thermal diffusivity. A static diffuse scattering component is observed in the γ -phase near the transition, and it can be attributed to remnant short-range ordering of the cations. Thermal conductivity modeling assessing the phonon scattering contributions from umklapp, boundary scattering, and point-defect mechanisms establishes a strong thermal conductivity suppression from the mass- and force-constant disorder on the Ag-Bi

cation sublattice, which is directly validated by our neutron scattering results. The present approach to control phonon linewidths in thermoelectrics via cation ordering, and measuring them *in-situ* with INS, opens an avenue to manipulate and probe fundamental processes of phonon scattering. This work explicitly highlights the impact of tunable microstructure on phonon scattering rates and thermal conductivity, providing insights on coupling phonon scattering mechanisms to optimize thermal transport for rational material design.

ACKNOWLEDGMENTS

J.N. wishes to acknowledge useful discussions with N. P. Luciano and J. Ma, technical support from D. Dunning, S. Elorfi, and E. Huckabay, and manuscript reviews by L. Lindsey and M. B. Stone. Neutron scattering measurements and analysis (J.N., C.L, O.D.) were supported as part of the S3TEC EFRC, an Energy Frontier Research Center funded by the US Department of Energy, Office of Science, Basic Energy Sciences under Award No. DE-SC0001299. First-principles simulations (D.B.) were supported by the US Department of Energy, Office of Science, Basic Energy Sciences, Materials Sciences and Engineering Division, under the Early Career Award No. DE-SC0016166 (PI O.D.) Thermal conductivity modeling (JD) and thermal measurements (TLA) were supported by the US Department of Energy, Office of Science, Basic Energy Sciences, Materials Sciences and Engineering Division, under Award No. DE-SC0019299. Sample synthesis (A.F.M.) was supported by the US Department of Energy, Office of Science, Basic Energy Sciences, Materials Sciences and Engineering Division. H.W. was supported by the Propulsion Materials program of Vehicle Technology Office under EERE. The research at Oak Ridge National Laboratory was sponsored by the Scientific User Facilities Division, Office of Basic Energy Sciences, US Department of Energy. Theoretical calculations were performed using resources of the National Energy Research Scientific Computing Center, a US DOE Office of Science User Facility supported by the Office of Science of the US Department of Energy under Contract No. DE-AC02-05CH11231. We acknowledge the support of the National Institute of Standards and Technology, US Department of Commerce, in providing the neutron research facilities used in this work.

J.L.N., D.B., C.L., and O.D. performed neutron scattering experiments with assistance from D.L.A., G.E., A.H., D.P., and J.W.L. J.L.N. analyzed all neutron data, including resolution deconvolution steps. First-principles simulations were performed by D.B. and J.D. Sample synthesis was performed by A.F.M. H.W. performed the thermal diffusivity measurements. T.L.A. performed heat capacity measurements. Resolution estimation software was written by J.Y.Y.L. J.L.N. and O.D. wrote the manuscript with input and review from all authors. O.D. supervised the project.

- [1] C. Wood, *Rep. Prog. Phys.* **51**, 459 (1988).
 [2] G. Chen, M. S. Dresselhaus, G. Dresselhaus, J. P. Fleurial, and T. Caillat, *Int. Mater. Rev.* **48**, 45 (2003).

- [3] G. J. Snyder and E. S. Toberer, *Nat. Mater.* **7**, 105 (2008).
 [4] H. J. Goldsmid, *Introduction to Thermoelectricity*, Springer Series in Materials Science Vol. 121 (Springer, Berlin, 2010).

- [5] J. He and T. M. Tritt, *Science* **357**, eaak9997 (2017).
- [6] W. Liu, J. Hu, S. Zhang, M. Deng, C.-G. Han, and Y. Liu, *Mater. Today Phys.* **1**, 50 (2017).
- [7] E. F. Hockings, *J. Phys. Chem. Solids* **10**, 341 (1959).
- [8] D. T. Morelli, V. Jovovic, and J. P. Heremans, *Phys. Rev. Lett.* **101**, 035901 (2008).
- [9] M. D. Nielsen, V. Ozolins, and J. P. Heremans, *Energy Environ. Sci.* **6**, 570 (2013).
- [10] K. F. Hsu, S. Loo, F. Guo, W. Chen, J. S. Dyck, C. Uher, T. Hogan, E. K. Polychroniadis, and M. G. Kanatzidis, *Science* **303**, 818 (2004).
- [11] L. Pan, D. Bérardan, and N. Dragoe, *J. Am. Chem. Soc.* **135**, 4914 (2013).
- [12] S. N. Guin, V. Srihari, and K. Biswas, *J. Mater. Chem. A* **3**, 648 (2014).
- [13] C. Xiao, X. Qin, J. Zhang, R. An, J. Xu, K. Li, B. Cao, J. Yang, B. Ye, and Y. Xie, *J. Am. Chem. Soc.* **134**, 18460 (2012).
- [14] D. S. Parker, A. F. May, and D. J. Singh, *Phys. Rev. Appl.* **3**, 064003 (2015).
- [15] F. Böcher, S. P. Culver, J. Peilstöcker, K. S. Weldert, and W. G. Zeier, *Dalton Trans.* **46**, 3906 (2017).
- [16] S. Mitra and D. Bérardan, *Cryst. Res. Technol.* **52**, 1700075 (2017).
- [17] J. Ma, O. Delaire, A. F. May, C. E. Carlton, M. A. McGuire, L. H. VanBebber, D. L. Abernathy, G. Ehlers, T. Hong, A. Huq, W. Tian, V. M. Keppens, Y. Shao-Horn, and B. C. Sales, *Nat. Nanotechnol.* **8**, 445 (2013).
- [18] J. Ma, O. Delaire, E. D. Specht, A. F. May, O. Gourdon, J. D. Budai, M. A. McGuire, T. Hong, D. L. Abernathy, G. Ehlers, and E. Karapetrova, *Phys. Rev. B* **90**, 134303 (2014).
- [19] E. D. Specht, J. Ma, O. Delaire, J. D. Budai, A. F. May, and E. A. Karapetrova, *J. Electron. Mater.* **44**, 1536 (2014).
- [20] C. E. Carlton, R. De Armas, J. Ma, A. F. May, O. Delaire, and Y. Shao-Horn, *J. Appl. Phys.* **115**, 144903 (2014).
- [21] L. Aggarwal, J. S. Sekhon, S. N. Guin, A. Arora, D. S. Negi, R. Datta, K. Biswas, and G. Sheet, *Appl. Phys. Lett.* **105**, 113903 (2014).
- [22] J. Zhang, X. Qin, D. Li, C. Song, Y. Liu, H. Xin, T. Zou, and Y. Li, *Electron. Mater. Lett.* **11**, 133 (2015).
- [23] B. Du and X. Tang, *J. Electron. Mater.* **44**, 2118 (2015).
- [24] C. Manolikas and J. Spyridelis, *Mater. Res. Bull.* **12**, 907 (1977).
- [25] S. Geller and J. H. Wernick, *Acta Crystallogr.* **12**, 46 (1959).
- [26] A. C. Glatz and A. Pinella, *J. Mater. Sci.* **3**, 498 (1968).
- [27] O. Delaire, J. Ma, K. Marty, A. F. May, M. A. McGuire, M.-H. Du, D. J. Singh, A. Podlesnyak, G. Ehlers, M. D. Lumsden, and B. C. Sales, *Nat. Mater.* **10**, 614 (2011).
- [28] P.-F. Lory, S. Pailhès, V. M. Giordano, H. Euchner, H. D. Nguyen, R. Ramlau, H. Borrmann, M. Schmidt, M. Baitinger, M. Ikeda, P. Tomeš, M. Mihalkovič, C. Allio, M. R. Johnson, H. Schober, Y. Sidis, F. Bourdarot, L. P. Regnault, J. Ollivier, S. Paschen, Y. Grin, and M. Boissieu, *Nat. Commun.* **8**, 491 (2017).
- [29] J. Y. Y. Lin, H. L. Smith, G. E. Granroth, D. L. Abernathy, M. D. Lumsden, B. Winn, A. A. Aczel, M. Aivazis, and B. Fultz, *Nucl. Instrum. Methods Phys. Res., Sect. A* **810**, 86 (2016).
- [30] S. V. Barabash, V. Ozolins, and C. Wolverton, *Phys. Rev. Lett.* **101**, 155704 (2008).
- [31] G. L. Squires, *Introduction to the Theory of Thermal Neutron Scattering*, 3rd ed. (Cambridge University Press, Cambridge, 2009).
- [32] P. Brüesch, *Phonons: Theory and Experiments* (Springer-Verlag, Heidelberg, 1982).
- [33] G. P. Srivastava, *The Physics of Phonons* (Taylor and Francis, New York, 1990).
- [34] A. A. Maradudin and A. E. Fein, *Phys. Rev.* **128**, 2589 (1962).
- [35] R. A. Cowley, *Rep. Prog. Phys.* **31**, 123 (1968).
- [36] See Supplemental Material at <http://link.aps.org/supplemental/10.1103/PhysRevMaterials.4.105402> for additional details on synthesis, characterization, data analysis, and resolution corrections.
- [37] J. W. Lynn, Y. Chen, S. Chang, Y. Zhao, S. Chi, W. Ratcliff II, B. G. Ueland, and R. W. Erwin, *J. Res. Natl. Inst. Stand. Technol.* **117**, 60 (2012).
- [38] D. L. Abernathy, M. B. Stone, M. J. Loguillo, M. S. Lucas, O. Delaire, X. Tang, J. Y. Y. Lin, and B. Fultz, *Rev. Sci. Instrum.* **83**, 015114 (2012).
- [39] G. Ehlers, A. A. Podlesnyak, J. L. Niedziela, E. B. Iverson, and P. E. Sokol, *Rev. Sci. Instrum.* **82**, 085108 (2011).
- [40] D. L. Abernathy, J. L. Niedziela, and M. B. Stone, *EPJ Web Conf.* **83**, 03001 (2015).
- [41] M. B. Stone, J. L. Niedziela, M. J. Loguillo, M. A. Overbay, and D. L. Abernathy, *Rev. Sci. Instrum.* **85**, 085101 (2014).
- [42] M. B. Stone, J. L. Niedziela, M. A. Overbay, and D. L. Abernathy, *EPJ Web Conf.* **83**, 03014 (2015).
- [43] O. Arnold, J. C. Bilheux, J. M. Borreguero, A. Buts, S. I. Campbell, L. Chapon, M. Doucet, N. Draper, R. Ferraz Leal, M. A. Gigg, V. E. Lynch, A. Markvardsen, D. J. Mikkelson, R. L. Mikkelson, R. Miller, K. Palmen, P. Parker, G. Passos, T. G. Perring, P. F. Peterson, S. Ren, M. A. Reuter, A. T. Savici, J. W. Taylor, R. J. Taylor, R. Tolchenov, W. Zhou, and J. Zikovsky, *Nucl. Instrum. Methods Phys. Res., Sect. A* **764**, 156 (2014).
- [44] R. Ewings, A. Buts, M. Le, J. van Duijn, I. Bustinduy, and T. Perring, *Nucl. Instrum. Methods Phys. Res., Sect. A* **834**, 132 (2016).
- [45] P. Brüesch, *Phonons: Theory and Experiments I*, Springer Series in Solid-State Sciences Vol. 34 (Springer, Berlin, 1982).
- [46] M. B. Stone, J. L. Niedziela, D. L. Abernathy, L. DeBeer-Schmitt, G. Ehlers, O. Garlea, G. E. Granroth, M. Graves-Brook, A. I. Kolesnikov, A. Podlesnyak, and B. Winn, *Rev. Sci. Instrum.* **85**, 045113 (2014).
- [47] M. Kresch, O. Delaire, R. Stevens, J. Y. Y. Lin, and B. Fultz, *Phys. Rev. B* **75**, 104301 (2007).
- [48] A. Huq, J. P. Hodges, O. Gourdon, and L. Heroux, *Z. Kristallogr. Proc.* **1**, 127 (2011).
- [49] A. C. Larson and R. B. Von Dreele, *GSAS General Structure Analysis System, Report LAUR 86-748* (Los Alamos National Laboratory, 1986).
- [50] G. Kresse and J. Hafner, *Phys. Rev. B* **47**, 558 (1993).
- [51] G. Kresse and J. Furthmüller, *Phys. Rev. B* **54**, 11169 (1996).
- [52] G. Kresse and J. Furthmüller, *Comput. Mater. Sci.* **6**, 15 (1996).
- [53] J. P. Perdew and A. Zunger, *Phys. Rev. B* **23**, 5048 (1981).
- [54] J. P. Perdew, K. Burke, and M. Ernzerhof, *Phys. Rev. Lett.* **77**, 3865 (1996).

- [55] A. Togo and I. Tanaka, *Scr. Mater.* **108**, 1 (2015).
- [56] F. Bao, R. Archibald, J. L. Niedziela, D. Bansal, and O. Delaire, *Nanotechnology* **27**, 484002 (2016).
- [57] M. Popovici, *Acta Crystallogr., Sect. A: Cryst. Phys., Diffr., Theor. Gen. Crystallogr.* **31**, 507 (1975).
- [58] E. Farhi, Y. Debab, and P. Willendrup, *J. Neutron Res.* **17**, 5 (2013).
- [59] Y. M. Shykeev, Y. A. Yusibov, M. B. Babanly, and B. A. Popovkin, *Russ. J. Inorg. Chem.* **48**, 1941 (2003).
- [60] T. M. Tritt, *Thermal Conductivity: Theory, Properties, and Applications* (Springer Science and Business Media, New York, 2005).
- [61] H. J. Maris, *Phys. Rev. B* **41**, 9736 (1990).
- [62] I. Yu, B. Ravich, and I. Smirnov, *Semiconducting Lead Chalcogenides* (Plenum, New York, 1970).
- [63] Y. Zhang, X. Ke, C. Chen, J. Yang, and P. R. C. Kent, *Phys. Rev. B* **80**, 024304 (2009).
- [64] P. A. Sharma, J. S. Ahn, N. Hur, S. Park, S. B. Kim, S. Lee, J.-G. Park, S. Guha, and S-W. Cheong, *Phys. Rev. Lett.* **93**, 177202 (2004).
- [65] Y.-L. Pei and Y. Liu, *J. Alloys Compd.* **514**, 40 (2012).
- [66] A. El-Sharkawy, A. A. El-Azm, M. Kenawy, A. Hillal, and H. Abu-Basha, *Int. J. Thermophys.* **4**, 261 (1983).
- [67] H. Wang, Y. Pei, A. D. LaLonde, and G. J. Snyder, *Proc. Natl. Acad. Sci. (USA)* **109**, 9705 (2012).